The Hurst exponent of *Fermi* gamma-ray bursts

G. A. MacLachlan,[1]★ A. Shenoy,[1] E. Sonbas,[2,3] R. Coyne,[1] K. S. Dhuga,[1]
A. Eskandarian,[1] L. C. Maximon[1] and W. C. Parke[1]

[1]*Department of Physics, The George Washington University, Washington, DC 20052, USA*
[2]*Department of Physics, University of Adiyaman, 02040 Adiyaman, Turkey*
[3]*NASA Goddard Space Flight Center, Greenbelt, MD 20771, USA*

ABSTRACT

Using a wavelet decomposition technique, we have extracted the Hurst exponent for a sample of 46 long and 22 short gamma-ray bursts (GRBs) detected by the Gamma-ray Burst Monitor aboard the *Fermi* satellite. This exponent is a scaling parameter that provides a measure of long-range behaviour in a time series. The mean Hurst exponent for the short GRBs is significantly smaller than that for the long GRBs. The separation may serve as an unbiased criterion for distinguishing short and long GRBs.

Key words: methods: data analysis – methods: statistical – gamma-ray burst: general.

1 INTRODUCTION

Our present understanding of complex astrophysical objects such as cataclysmic variables (CVs), active galactic nuclei and gamma-ray bursts (GRBs) comes nearly entirely from the temporal and spectral analyses of their photoemissions (with some additional information coming from possible associations, such as host galaxies). In this paper, we consider the temporal aspects of GRB light curves observed by the Gamma-Ray Burst Monitor (GBM) aboard the *Fermi* satellite. Many studies of the temporal properties of GRB light curves have been published, such as Nemiroff (2000, 2012), Norris et al. (2005), Hakkila & Nemiroff (2009) and Hakkila & Preece (2011), from the perspective that light curves are comprised of a series of displaced pulses and that by fitting the individual pulses and associating pulses at various photon energies one can arrive at a holistic understanding of light curves which in turn may be used to constrain the physics of the engines that produce them. The main appeal of this approach is the intuitive connection between pulses and collisions in the internal shock model. While this is a perfectly reasonable method, issues do arise concerning the functional form to use for pulse fitting and how to discern actual pulses from stochastic fluctuations in the light curves. The situation is further exacerbated by the fact that GRB light curves exhibit considerable variation in duration and in pulse profile. We note the significant progress made in non-parametric analyses using the Bayesian block technique (Scargle et al. 2012). In this type of analysis, the duration of a light curve is represented as a tessellated block of time which can be partitioned into a complete array of sub-blocks in any number of ways. An optimal partition (a partition of sub-blocks maximizing a fitness function) is shown to exist, be unique and computable iteratively. The optimal partition of sub-blocks is

determined, given a prior probability distribution for the number of blocks, by finding the model best representing the data as sets of piecewise constant segments or sub-blocks. This technique shows great promise in resolving statistically significant temporal features from noise and detector related artefacts.

An ideal complementary approach to probing light curves would be one which handles seemingly disparate profiles on an equal footing and distils their complex forms into a single parameter which may be used to compare one light curve with another. One such method was pioneered by Harold Edwin Hurst (Hurst 1951) with a technique he invented called the rescaled range analysis (R/S) which was later improved upon by Benoit Mandelbrot (Mandelbrot & van Ness 1968). The eponymous parameter resulting from the R/S is called the Hurst exponent, *H*, and is closely related to the fractal dimension, *D*, the understanding of which Mandelbrot spent much of his career developing. In fact, fractional Brownian motion (fBm), which Mandelbrot defined in 1968, is parametrized solely by *H* and serves as a useful model for discussing time series. After determining *H* for a given time series, one is in a position to make several statements about the nature of that time series including whether the sequence appears random or whether it is persistent or antipersistent, and if so, whether it exhibits long-range dependence, and over what time-scales these characteristics are operative. All of these are informative quantitative statements, especially if the specific process generating the time series is partially or completely unknown, in which case, these statements are perhaps all one can really say about the process given the available information. Some fields of research in which interesting work is being done with Hurst exponents are financial markets, seismology, anaesthesiology, astrophysics, plasma physics and genomics.

We point out that neither the pulse-fitting methods nor the Bayesian block analysis (Scargle et al. 2012) yields information directly relatable to the Hurst exponent as does the wavelet analysis. One approach to access the Hurst exponent from a Bayesian

★ E-mail: maclach@gwu.edu

block framework that seems reasonable would be an adaptation of the box-counting algorithm (Feder 1988). Such a Bayesian box-counting algorithm is outside the scope of this paper.

The estimation of the Hurst exponent and the related scaling exponent, α, has a history in astrophysics (Fritz & Bruch 1998; Walker & Schaefer 2000; Tamburini, De Martino & Bianchini 2009; Anzolin et al. 2010) for both CVs and GRBs. We propose that a similar determination of H for GRB light curves will be a valuable tool for categorization and we present a separation of long and short GRBs based on H.

2 METHODOLOGY

2.1 Hurst exponent and self-affinity

Pioneering work in self-similarity and long-range dependence was first published in 1951 by Hurst in the study of annual Nile River levels, (Hurst 1951). Hurst examined several decades of data to determine what should be the minimum size of a reservoir so that it neither overflows nor runs dry due to yearly fluctuations and made the unexpected observation that annual Nile River levels were not independent from one another but instead exhibited a *memory* of past events.

In this analysis of time series data, we search for statistical fractals, i.e. fractals whose statistical characteristics are independent of time-scale. Such fractal time series are called *self-similar*. There is another class of statistical fractals whose scale invariance is broken but can be restored by a multiplicative factor. These statistical fractals are called *self-affine*. Mandelbrot & van Ness (1968) defined a time series, $X(t)$ with $t \in \{t_0, \ldots, t_{N-1}\}$, to be self-affine if, after a rescaling $t \to \lambda t$, the following relation is satisfied,

$$X(t) \doteq \lambda^{-H} X(\lambda t). \tag{1}$$

The exponent, H, is the Hurst exponent (Hurst 1951) and the symbol $\doteq$ denotes equality in distribution. The canonical example of a self-affine time series, also given by Mandelbrot & van Ness (1968), is fBm. Stationary in the context of this paper is second-order stationarity which means the first and second moments obey the following relations:

$$\mathbb{E}\{X(t)\} = \mu_X$$
$$\mathbb{E}\{X(t_2)X(t_1)\} = \gamma(t_2 - t_1) = \gamma(\tau), \tag{2}$$

where μ_X is the sample mean, γ is the autocovariance sequence and $\tau \equiv t_2 - t_1$ is the lag. The Hurst exponent, H, parametrizes the degree of statistical self-similarity which a time series exhibits. A self-similar series may be sub-divided into three categories: A series with $1/2 < H < 1$ is referred to as persistent or long-range dependent while a series with $0 < H < 1/2$ is referred to as antipersistent, Feder (1988). For $H = 1/2$, we have neither persistence nor antipersistence and this corresponds to the case of random and uncorrelated events. The Hurst exponent provides a model-independent characterization of the data. Three examples of times series with different values of H are shown in Fig. 1. A graphical depiction of the rescaling described by equation (1) for a time series with $H = 0.25$ is given in Fig. 2 and for a time series with $H = 0.75$ in Fig. 3.

2.2 Wavelet transforms

Wavelet transformations have been shown to be a natural tool for multiresolution analysis of non-stationary time series (Mallat 1989; Flandrin 1992). Wavelet analysis is similar to Fourier analysis in
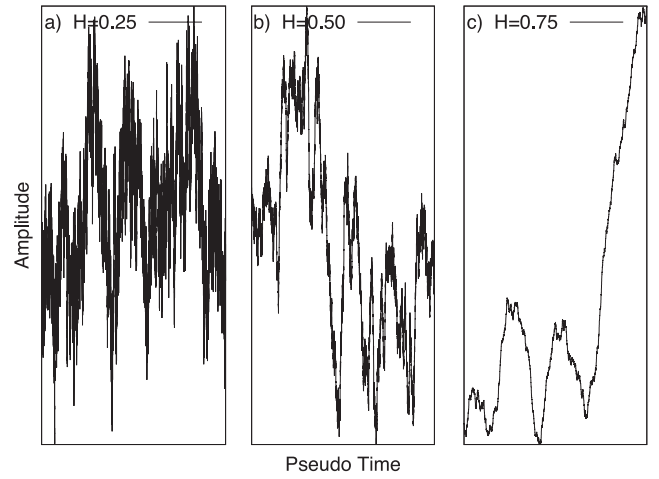

Figure 1. Simulated fBms with different values of H: (a) $H = 0.25$, (b) $H = 0.50$, (c) $H = 0.75$.

Figure 2. Graph of $B_H(t)$ with $H = 0.25$. A box is placed around a sub-range of t (lower-left corner). The box is zoomed into with time axis scaled by a and amplitude scaled by a^{-H}. This is a *self-affine* transformation that not only makes the rescaled version qualitatively 'similar' to the original but also preserves the variance as computed in equation (9).
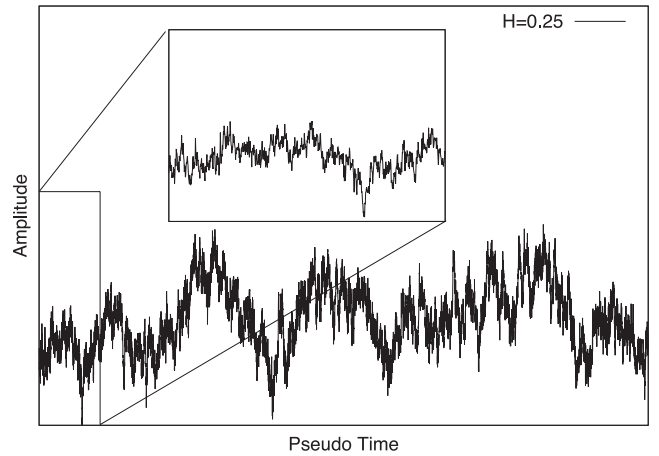

Figure 3. Graph of $B_H(t)$ with $H = 0.75$. A box is placed around a sub-range of t (lower-left corner). The box is zoomed into with time axis scaled by a and amplitude scaled by a^{-H}. This is a *self-affine* transformation that not only makes the rescaled version qualitatively 'similar' to the original but also preserves the variance as computed in equation (9).
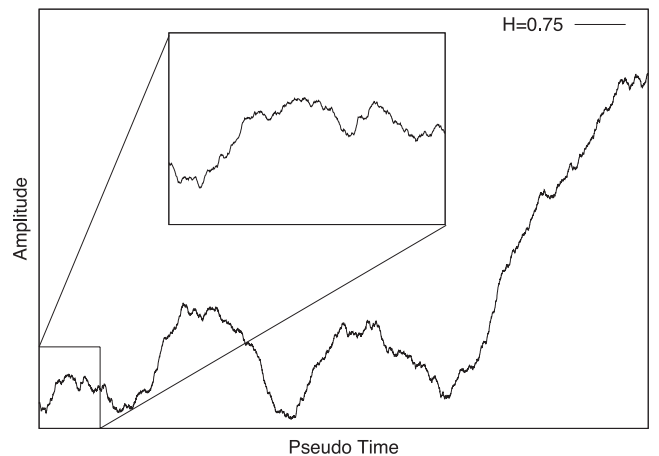
many respects but differs in that a wavelet basis function, $\psi(t)$, is well localized while Fourier basis functions are global. Localization means that outside some range the amplitudes of wavelet basis functions go to zero or are otherwise negligibly small, Percival (2000). On the other hand, the wavelet transform is similar to the Fourier transform because they both are expansions into a complete orthogonal basis and resolve low-frequency, large-scale structure from high-frequency, small-scale structure.

Wavelet analysis is said to be multiresolution because the time series under investigation is interrogated at multiple scales by a basis set of wavelets which are rescaled and translated versions of an original wavelet commonly referred to as the mother wavelet, $\psi(t)$,

$$\psi(t) \rightarrow \psi_{a,b}(t) = \frac{1}{\sqrt{a}}\psi\left(\frac{t-b}{a}\right), \tag{3}$$

where a represents an octave or time-scale and the parameter b gives the position of the wavelet within the octave.

The continuous wavelet transform (CWT) coefficient, $C_{a,b}$, of a time series for some scale and position is computed as

$$C_{a,b} = \frac{1}{\sqrt{a}} \int X(t)\psi_{a,b}(t)\,\mathrm{d}t. \tag{4}$$

2.2.1 Wavelet analysis

The wavelet-transform technique for estimating self-affinity is outlined here. By substituting the distribution relation in equation (1) into equation (4), we find

$$\begin{aligned} C_{a,b} &= \frac{1}{\sqrt{a}} \int X(t)\psi_{a,b}(t)\,\mathrm{d}t \\ &= \frac{\lambda^{-(H+1/2)}}{\sqrt{\lambda a}} \int X(\lambda t)\psi_{a,b}\left(\frac{\lambda t - \lambda b}{\lambda a}\right)\,\mathrm{d}(\lambda t) \\ &= \lambda^{-(H+1/2)}C_{\lambda a, \lambda b}. \end{aligned} \tag{5}$$

It is straightforward to see from equation (5) that a self-affine time series will have wavelet coefficients whose variance over a particular scale, λa, is related to the scale parameter λ by

$$\log \mathrm{var}(C_{\lambda a, \lambda b}) = (2H+1)\log\lambda + \text{constant}. \tag{6}$$

2.2.2 Fast wavelet transform

Similar to the CWT, the discrete fast wavelet transform (FWT) is also a multiresolution operation owing to the construction of the wavelets, $\psi_{j,k}$, which form the basis of the discrete FWT. We employed the discrete wavelet transform because of its high degree of computational efficiency. In order to distinguish between the CWT and its FWT counterpart, we make a slight change of notation. Just as before, the $\psi_{j,k}$, are rescaled, translated versions of the mother wavelet, ψ,

$$\psi_{j,k} = 2^{-j/2}\psi(2^{-j}t - k). \tag{7}$$

The coefficients of the FWT are written as

$$d_{j,k} = \langle X, \psi_{j,k}\rangle,$$

where j and k play the roles of a and b, respectively. Moreover, the values which j and k assume obey the dyadic partitioning scheme

(Mallat 1989; Percival 2000; Addison 2002). That is, for a time series whose number of elements is given by $N = 2^m$,

$$0 \le j \le m - 1$$

and

$$0 \le k \le 2^j - 1.$$

Applying the dyadic partitioning scheme removes any redundant encoding of information by the wavelet-transform coefficients and guarantees orthogonality among the wavelet basis for any change in j or k,

$$\langle \psi_{j,k}, \psi_{j',k'}\rangle = \delta_{j,j'}\delta_{k,k'}. \tag{8}$$

2.3 Log-scale diagrams

The average power of the light curve at time-scale j is expressed as β_j and may be written in terms of the variance of the FWT coefficients as

$$\beta_j = \mathrm{var}(d_{j,k}) = \frac{1}{n_j}\sum_{k=0}^{n_j-1}|d_{j,k}|^2, \tag{9}$$

where n_j is the number of coefficients at scale j (Abry et al. 2000, 2003). Similarly to equation (6), it has been shown by Flandrin (1992) that for a series with non-stationary statistics the power-law variance of wavelet coefficients goes like

$$\log_2(\beta_j) = (2H+1)j + \text{constant}, \tag{10}$$

where H is the Hurst exponent. Masry (1993) later extended this result to a larger class of non-stationary problems with stationary increments in the low-frequency limit and showed that fBms are a special case. A plot of equation (10) is referred to as a log-scale diagram. Log-scale diagrams are useful for identifying scaling regions, i.e. the range of octaves over which self-affine scaling occurs. The slope, α, of the scaling region is related to the Hurst exponent through $\alpha = 2H + 1$.

In practice, a piecewise fitting function, $f(j; p_i)$ is defined as

$$f(j; p_i) = \begin{cases} p_1; & 1 \le j \le p_0 \\ p2 + p_3 j; & p_0 \le j \end{cases},$$

where p_0 is the value of j at which the piecewise fitting function changes definition.

2.4 Choice of wavelet basis

As in any orthogonal transformation, the basis functions to use in a wavelet transform is a matter of strategic choice. One typically chooses a basis that emphasizes some characteristic of interest. Commonly used families of wavelet bases are the Coiflet, Daubechies and Haar (Addison 2002). We chose the Haar wavelet basis which is the simplest of the Daubechies family.

The Haar wavelet basis was chosen from among all other possible bases because it has the fewest number of vanishing moments and most compact support (Addison 2002), has a straightforward interpretation, i.e. is equivalent to the Allan variance (Xizheng & Zhensen 1997), and is constant over its interval of support similar to the model assumed in the Bayesian block method (Scargle 1998; Scargle et al. 2012).

The Haar basis is not without some defects, as noted by Kaplan & Jay Kuo (1993) and Flandrin (1992). Namely the Haar wavelet transformation is known to underestimate the actual Hurst exponent

and this phenomenon is a function of the coarseness of the binning, the number of counts in the light curve and also of H itself. We show in Section 2.6 that this effect is present but smaller than $\approx 1\sigma$ for a set of simulated light curves and is likely to be smaller for actual data. However, we consider that the advantages of the Haar basis outweigh its disadvantages.

2.5 Minimizing uncertainties

2.5.1 Circular permutation

Spurious artefacts due to incidental symmetries resulting from accidental misalignment (Coifman 1995; Percival 2000) of light curves with wavelet basis functions are minimized by circularly shifting the light curve against the basis functions. Circular shifting is a form of translation invariant de-noising (Coifman 1995). It is possible that a shift will introduce additional artefacts by moving a different symmetry into a susceptible location. The best approach is to circulate the signal through all possible values, or at least a representative sampling, and then take an average over the cases which minimizes the effect of spurious correlations.

2.5.2 Reverse-tail concatenation

Both discrete Fourier and discrete wavelet transformations imply that the expansion is periodic, with the longest period equal to the full time range of the input data. This can be interpreted to mean that for a series of N elements, $\{X_0, X_1, \ldots, X_{N-1}\}$, X_0 is made a surrogate for X_N and X_1 is made a surrogate for X_{N+1}, and so forth. This assumption may lead to trouble if X_0 is much different from X_{N-1}. In this case, artificially large variances may be computed. Reverse-tail concatenation minimizes this problem by making a copy of the series which is then reversed and concatenated on to the end of the original series resulting in a new series with a length twice that of the original. Instead of matching boundary conditions like,

$$X_0, X_1, \ldots, X_{N-1}, X_0, \tag{11}$$

we match boundaries as,

$$X_0, X_1, \ldots, X_{N-1}, X_{N-1}, \ldots, X_1, X_0. \tag{12}$$

Note that the series length has thus artificially been increased to $2N$ by reversing and doubling of the original series. Consequently, the wavelet variances at the largest scale in a log-scale diagram reflect this redundancy. This is the reason that the wavelet variances at the largest scale are excluded from least-squares fits of the scaling region.

2.5.3 Poisson operator

Photon counting statistics are considered in a bootstrapping procedure by applying a Poisson operator, $\mathcal{P}(\lambda_i, X_i)$, to every light curve prior to analysing. Each light curve is binned initially at 200 μs and the number of counts per bin, X_i, is used as a mean value, λ_i, to be supplied to a Poisson random number generator. The value returned from $\mathcal{P}(\lambda_i, X_i)$ is used to replace the number of counts stored in X_i. The Poisson operator is applied to the signal X_i prior to every circular permutation. We show in Section 2.6 that the Poisson operator does not affect the measured slope of log-scale diagrams above the Poisson level.

2.6 A test case: fBm

Spatial-temporal fBms are a useful model for studying self-similarity and long-range dependence in non-stationary time series (Mandelbrot & van Ness 1968) and are characterized by a single parameter, H, the Hurst exponent. An fBm with a particular H is expressed as $B_H(t)$ and has the property of self-similarity over a range of scales after a rescaling of axes,

$$B_H(t) \doteq a^{-H} B_H(at), \tag{13}$$

where $\doteq$ denotes distributional equality as in Section 2.1. The efficacy of the H estimation procedure was tested using simulated data in the form of fBm time series. Two tests were performed; in the first test, we examine the ability of our algorithm to determine H from fBms in the presence of Poisson noise and in the second test we examine how well we can determine H at $H = 0.25$, 0.50 and 0.75 from noise-free fBms.

2.6.1 Test 1

The numerical computing environment MATLAB was used to produce 1000 realizations of fBms with scaling parameter H randomly chosen from the range $0.0 < \alpha < 1.0$ by using a uniform random number generator. Copies of the fBms were combined with a Poisson operator as described in Section 2.5.3. The fBms and the Poissonian fBms thus produced are shown in black and red, respectively, in panel (a) of Fig. 4. Panel (b) shows the Poisson noise that has been added by $\mathcal{P}$. The log-scale diagrams in panel (c) illustrate the effect of Poisson statistics on the Hurst exponent. The bare fBm is shown in black, the dressed Poisson-type fBm is in red and the residual Poisson noise in shown in blue. The log-scale diagram for the bare fBm in panel (c) exhibits a clean slope across all octaves. We see the effect of a Poisson noise operator; it adds to the signal variance constant across all octaves. Below some octave the signal is completely dominated by noise but above that octave the slope of the log-scale diagrams is independent of $\mathcal{P}$. See, for example, the black and red symbols for $j \geq 6$.

2.6.2 Test 2

In the second test, 3000 simulated Poisson-type light curves were generated. The simulated data were divided into three sub-groups of 1000 according to H. The three sub-groups were $H = \{0.25, 0.50, 0.75\}$. The simulated data in each group were analysed and an attempt was made to recover the value of the Hurst exponent, H, used to generate the fBm. The Hurst exponent was estimated by a least-squares fit to the scaling portion of the log-scale diagrams to determine α and then H is found from equation (10).

Results of the second test can be seen in Fig. 5 and Table 1. The results show that the FWT analysis with the Haar wavelet basis does underestimate the value of H as discussed in Section 2.4 but the magnitude of the error is not significant for our purpose.

3 DATA REDUCTION

The GBM on board *Fermi* observes GRBs in the energy range 8 keV–40 MeV. The GBM is composed of 12 thallium-activated sodium iodide (NaI) scintillation detectors (12.7 cm in diameter by 1.27 cm thick) that are sensitive to energies in the range of 8 keV–1 MeV and two bismuth germanate scintillation detectors (12.7 cm diameter by 12.7 cm thick) with energy coverage between 200 keV
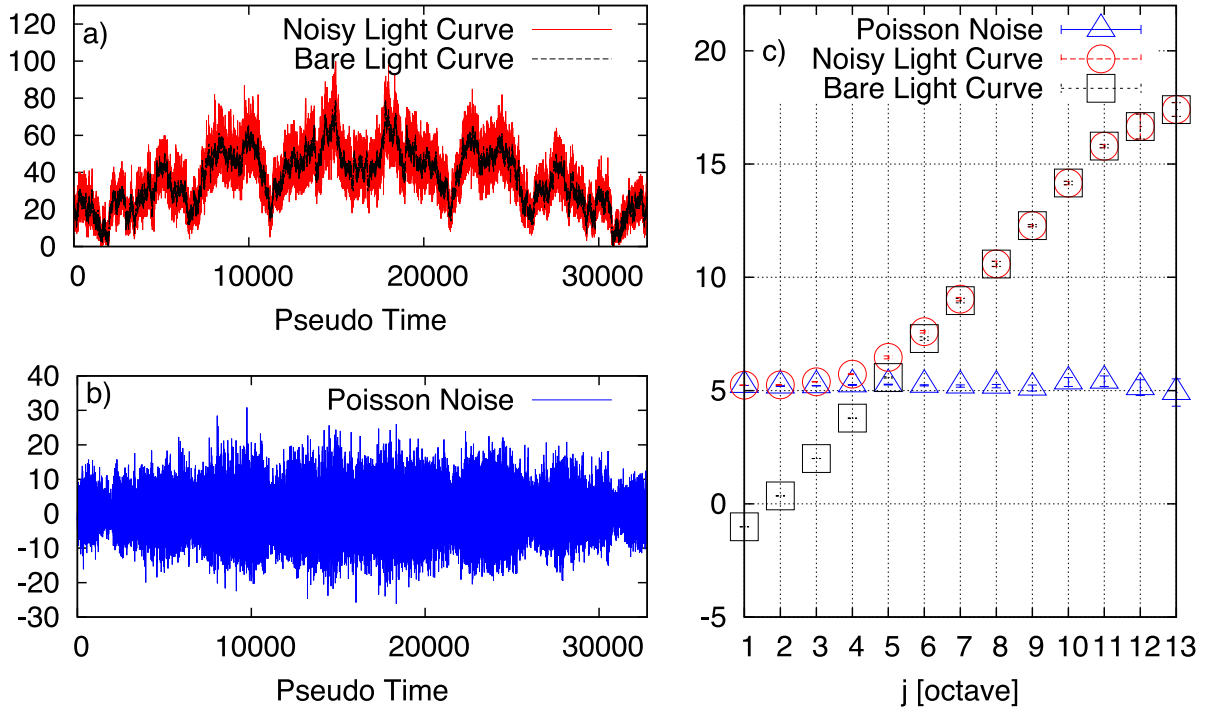
Figure 4. Panel (a) shows a sample fBm pre-processed and ready to be analysed in black and the same light curve after applying the Poisson operator, $\mathcal{P}$, in red. Panel (b) shows the Poisson noise that has been added by $\mathcal{P}$. In panel (c), log-scale diagrams illustrate the effect of Poisson statistics on the Hurst exponent. The bare fBm is shown in black, the dressed Poisson-type fBm is in red and the residual Poisson noise in shown in blue.
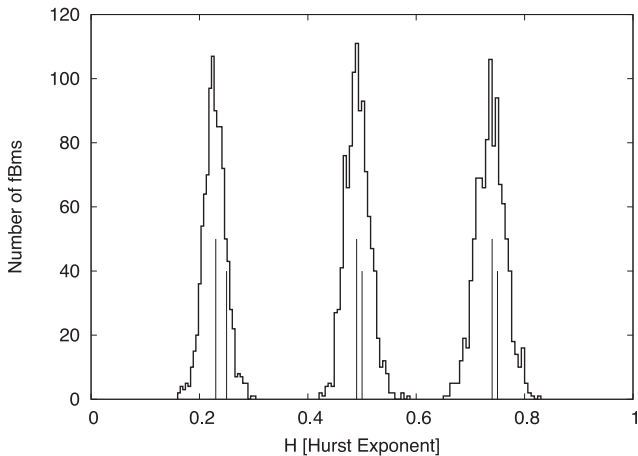

Figure 5. Histograms of 3000 simulated fBm traces. Three categories of fBms were generated with known Hurst exponents, $H = 0.25$, 0.50 and 0.75. These fBms were then analysed to recover the Hurst exponent. The histograms are the results of this analysis. Pairs of vertical lines are drawn for each peak. The shorter of the two indicates the known H used to generate the fBms and the longer of the two indicates the H extracted by our analysis. Results are tabulated in Table 1.

Table 1. Summary of results in Fig. 5.

H	H_{meas}
0.25	0.23 ± 0.02
0.50	0.49 ± 0.02
0.75	0.74 ± 0.03

and 40 MeV. The GBM detectors are arranged in such a way that they provide a significant view of the sky (Meegan et al. 2009).

In this work, we have extracted light curves for the GBM NaI detectors over the entire energy range (8 keV–1 MeV, also including the overflow beyond 1 MeV). Typically, the brightest three NaI detectors were chosen for the extraction. Light curves for both long and short GRBs were extracted at a time binning of 200 μs. The long GRBs were extracted over a duration starting from 20 s before the trigger and up to about 50 s after the T_{90} (taken from the *Fermi* GBM-Burst Catalog; Paciesas et al. 2012) for the burst without any background subtraction. For short GRBs, durations were chosen to be 20 s before the trigger and 10 s after the T_{90}. The T_{90} durations were obtained from the *Fermi* GBM-Burst Catalog (Paciesas et al. 2012). Summaries for the 46 long and 22 short GRBs used in this study are tabulated in Tables 2 and 3.

4 RESULTS AND DISCUSSION

We have used a technique based on wavelets to determine the Hurst exponents for a sample of GRB prompt-emission light curves. As noted in Section 2.1, the Hurst exponent provides a measure of correlated behaviour in a time series. The extreme values of H vary from 0 to 1, and a value of 0.5 implies uncorrelated (random) behaviour. As the fBm model indicates, large H-values tend to be associated with relatively smooth functions and small H-values tend to favour highly jagged curves. This feature suggests that H may be useful in quantifying the variability observed in GRB prompt-emission light curves. Plotted in Fig. 6 are the extracted H-exponents as histograms for both long and short GRBs. The histograms clearly show a displacement in H for the distributions of long and short GRBs, with the short GRBs indicating a preference for small values of H (see Table 4). The mean displacement in H raises the interesting possibility of using this feature as a way of distinguishing between

Table 2. Summary of long GRBs.

GRB Number	H	δH	T_{90} (s)	δT_{90} (s)
080723557	0.316	0.023	58.369	1.985
080723985	0.425	0.053	42.817	0.659
080724401	0.451	0.060	379.397	2.202
080804972	0.549	0.085	24.704	1.460
080806896	0.591	0.056	75.777	4.185
080807993	0.105	0.014	19.072	0.181
080810549	0.211	0.037	107.457	15.413
080816503	0.258	0.035	64.769	1.810
080817161	0.393	0.048	60.289	0.466
080825593	0.382	0.036	20.992	0.231
080906212	0.716	0.070	2.875	0.767
080916009	0.414	0.053	62.977	0.810
080925775	0.453	0.056	31.744	3.167
081009140	0.732	0.073	41.345	0.264
081101532	0.255	0.040	8.256	0.889
081125496	0.629	0.080	9.280	0.607
081129161	0.261	0.036	62.657	7.318
081215784	0.629	0.070	5.568	0.143
081221681	0.567	0.089	29.697	0.410
081222204	0.502	0.065	18.880	2.318
081224887	0.692	0.071	16.448	1.159
090102122	0.126	0.013	26.624	0.810
090131090	0.575	0.062	35.073	1.056
090202347	0.241	0.039	12.608	0.345
090323002	0.294	0.025	135.170	1.448
090328401	0.289	0.034	61.697	1.810
090411991	0.057	0.017	14.336	1.086
090424592	0.442	0.029	14.144	0.264
090425377	0.360	0.047	75.393	2.450
090516137	0.206	0.026	118.018	4.028
090516353	0.214	0.104	123.074	2.896
090528516	0.259	0.026	79.041	1.088
090618353	0.524	0.053	112.386	1.086
090620400	0.508	0.052	13.568	0.724
090626189	0.352	0.025	48.897	2.828
090718762	0.482	0.055	23.744	0.802
090809978	0.732	0.124	11.008	0.320
090810659	0.558	0.104	123.458	1.747
090829672	0.300	0.029	67.585	2.896
090831317	0.102	0.013	39.424	0.572
090902462	0.188	0.014	19.328	0.286
090926181	0.369	0.032	13.760	0.286
091003191	0.316	0.033	20.224	0.362
091127976	0.611	0.060	8.701	0.571
091208410	0.409	0.031	12.480	5.018
100414097	0.183	0.020	26.497	2.073

Table 3. Summary of short GRBs.

GRB Number	H	δH	T_{90} (s)	δT_{90} (s)
080723913	0.026	0.008	0.192	0.345
081012045	−0.022	−0.002	1.216	1.748
081102365	0.075	0.011	1.728	0.231
081105614	0.135	0.026	1.280	1.368
081107321	0.331	0.059	1.664	0.234
081216531	0.366	0.046	0.768	0.429
090108020	0.482	0.048	0.704	0.143
090206620	0.358	0.042	0.320	0.143
090227772	0.409	0.038	1.280	1.026
090228204	0.381	0.027	0.448	0.143
090308734	0.030	0.004	1.664	0.286
090429753	0.321	0.045	0.640	0.466
090510016	0.192	0.017	0.960	0.138
090621922	0.255	0.053	0.384	1.032
090907808	0.265	0.034	0.832	0.320
091012783	0.120	0.014	0.704	2.499
100117879	0.479	0.046	0.256	0.834
100204858	0.518	0.070	1.920	2.375
100328141	0.034	0.005	0.384	0.143
100612545	0.171	0.021	0.576	0.181
100625773	0.232	0.041	0.192	0.143
100706693	−0.031	−0.009	0.128	0.143
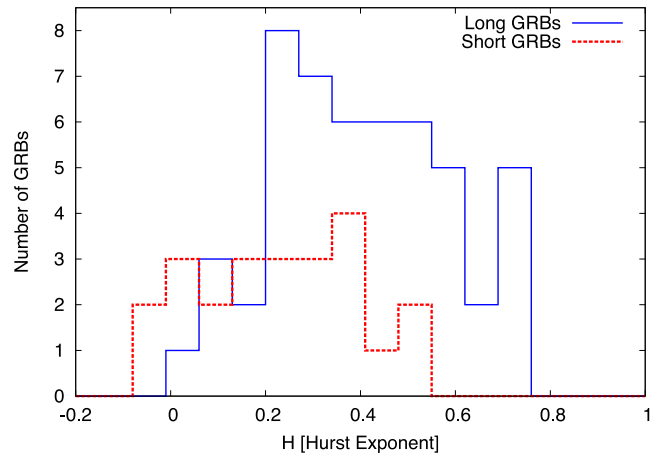
Figure 6. Histogram of H extracted from long and short GRBs. The result for long GRBs is plotted as the solid blue line while the short GRB result is plotted with the dashed red line. Note the overlap but also that the means are displaced from one another as shown in Table 4 for details of plot.

Table 4. Summary of results in Fig. 6.

Type	N	STD	$\langle H \rangle$
Long	46	0.18	0.40 ± 0.03
Short	22	0.17	0.23 ± 0.04

short and long GRBs. This would be in addition to the currently employed criteria based on T_{90} and spectral hardness ratios. Interestingly, the histograms also show a significant overlap in the region of small H-exponents possibly signalling similarities between the two types of bursts in this range.

It could be argued that the sizeable overlap of the distributions is essentially a consequence of the large dispersion (in H) exhibited by both short and long GRB distributions. While it is not known precisely what processes lead to this large dispersion in H, we note that the dispersion for the short GRBs is somewhat smaller than the corresponding one for long GRBs. If the dispersion is associated with the energetics of the progenitors of the respective systems, i.e. a merger of compact objects in the case of short GRBs and the collapse of a rapidly rotating massive star for long GRBs, then one might indeed expect a larger dispersion in the H-distribution

of long GRBs compared to the corresponding one for short GRBs based purely on the difference in the mass range for the respective progenitors. Moreover, additional factors such as the formation of an accretion disc, the size of the disc, the mass of the disc, the strength of the magnetic field and the magnitude of the accretion rate during the prompt phase, remain largely uncertain. With the added intrinsic variability of the central engine itself, we should not be surprised to observe a systematic difference in the extracted Hurst
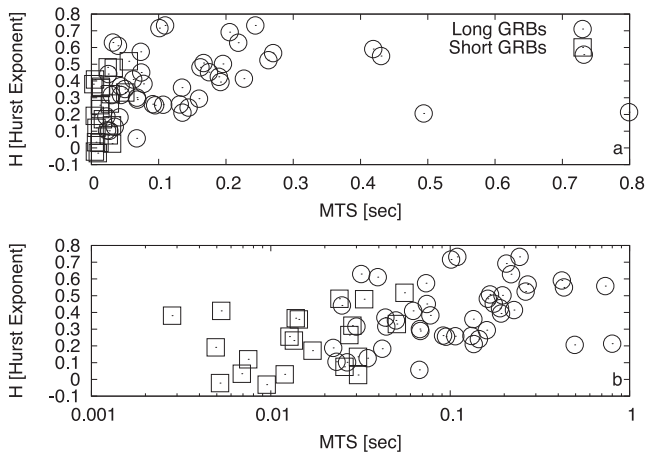
Figure 7. A scatter plot of *H* against the minimum variability time-scale from MacLachlan et al. (2012, 2013).

exponents for long and short bursts. For completeness, we mention that while the dispersion in *H* is large for both distributions, the extracted *H*-value for each individual GRB is known reasonably precisely (see Table 1).

Another way to examine the *H*-distributions is to recast the data against the so-called minimum-time-scale parameter, MTS, extracted by MacLachlan et al. (2012, 2013). Using a method based on wavelets, these authors explored the scaling characteristics of GRBs and determined the minimum time-scale at which scaling processes dominate over random noise processes. Furthermore, the authors have recently shown a direct connection between the extracted MTS and the smallest pulse structures extracted by pulse-fitting techniques. The same conclusions were confirmed independently by Bhat (2013) using a similar technique to extract MTS by computing rescaled Pearson variances. Furthermore, a link between pulse properties and MTS connecting GRB prompt emission and X-ray flaring has been identified by Sonbas et al. (2013).

In addition to this link with pulses, MTS provides an alternate scale (to T_{90}) by which long and short GRBs can be separated. Shown in Fig. 7 are the extracted *H*-exponents for both long and short GRBs versus the MTS (in the observer frame). Short GRBs tend to cluster around small MTS values and follow a steep trajectory in the *H*–MTS plane whereas the long GRBs are distributed over a larger range in MTS and seem to follow a gradual power-law-like trajectory. The behaviour is a little more clear in panel (b) of Fig. 7 where the MTS is plotted on a log scale: Here, the short and long GRBs indicate a small (∼30 per cent) positive correlation respectively; the combined sample on the other hand shows a larger positive correlation (∼50 per cent) and an obvious separation of the two distributions with MTS.

Other astrophysical systems for which the Hurst exponent has been extracted includes CVs. These systems, comprising tightly bound binaries (with periods of the order of few hours) and a primary consisting of a compact object (typically a white dwarf) and an accretion disc that can accommodate significant mass transfer from the secondary, may provide a benchmark for gauging the systematics of the extracted Hurst exponents. Indeed, large dispersions in *H* are found for both optical and X-ray light curves of CVs. Interestingly though, CVs apparently tend to favour large *H*-exponents, i.e. greater than 0.5. This implies that the CV distributions are persistent as opposed to a tendency towards antipersistence for GRBs. By their very nature, CVs are systems that have built-in periodicity that is readily reflected, in most cases, in the observed emissions from

these systems. GRBs, on the other hand, are transient phenomena which show very little evidence for periodicities. It is possible that this simple difference may lead, in part at least, to the degree of persistence or antipersistence exhibited by these systems. Furthermore, some authors, (Fritz & Bruch 1998; Tamburini et al. 2009; Anzolin et al. 2010), have noted that the extracted *H*-values indicate a sensitivity to the strength of the magnetic field of the systems under study, and in particular, the optical and X-ray emissions from CVs exhibit different *H*-distributions. Since the optical and X-ray emissions in CVs arise from spatially separated regions (the optical from an extended disc and the X-ray in the boundary layer between the inner regions of the disc and the surface of the compact object or the polar regions in the case of a highly magnetic system), it is tempting to surmise that such a comparison might be fruitful in elucidating the spatial characteristics of GRB jets: Examples include the radii and/or regions that are commonly associated with the emission sites for prompt gamma-rays (e.g. the photospheric radius in the case of a thermal component) and the steeply declining phase of the X-ray light curves (linked with high-latitude emission resulting from internal shell collisions). While it is understood that GRBs and CVs are very different systems and therefore the translation of the Hurst exponent from one system to the other is likely to be speculative at best, it is intriguing nonetheless that a simple scaling parameter may enable us to connect common underlying properties and processes that ultimately produce the observed emission in these diverse systems.

5 CONCLUSIONS

We have studied the temporal properties of a sample of prompt-emission light curves for short- and long-duration GRBs detected by the *Fermi*/GBM mission. By using a technique based on wavelets, we have extracted the Hurst exponents for these bursts. This exponent measures the relation between variability over the full range of available time-scales, comparing long-range with short-range variability. The physical limits of this index are 0 and 1, where the mid-point ($H = 0.5$), is an indicator of completely uncorrelated (random) processes that contribute to the observed time series. Often, the *H* is also associated with the fractal dimension (*D*) of structures by

$$D = 2 - H, \tag{14}$$

and can be thought of as a measure of the degree of jaggedness of the structures under study. In this sense, the *H* may also be indirectly linked to the variability seen in the prompt-emission of many GRBs. Our main results are summarized as follows.

(a) The means of the *H*-distributions for the GRBs in our sample show an offset between short and long GRBs, with the short GRBs indicating a preference for smaller Hurst exponents compared to the long GRBs. This offset is potentially an independent criterion for distinguishing between long- and short-duration bursts.

(b) Compared to short GRBs, long-duration bursts exhibit a larger dispersion in *H*. The origin of this dispersion is not known, although it is possible that it is related to the underlying energetics of the different progenitors that produce long- and short-duration bursts.

(c) No distinct group or clustering is found for *H*-values corresponding to 0.5. This implies that random (or uncorrelated) processes, if present, play a lesser role in the production of the observed prompt emission. Moreover, the means of the *H*-distributions for both long and short GRBs indicate a skewness towards values less

than 0.5. Overall, this implies that the prompt-emission time series exhibit antipersistence.

Finally, we note that because of the large dispersion in H, there exists a significant region over which the long and short bursts overlap. This overlap region raises the interesting possibility of exploring bursts that may possess many more common features than would otherwise be suspected. The case for an intermediate class of GRBs (Horvath 1998; Gao, Lu & Zhang 2010) remains unsettled and warrants further investigation.

ACKNOWLEDGEMENTS

REFERENCES

Abry P., Flandrin P., Taqqu M. S., Veitch D., 2000, in Park K., Willinger W., eds, Self-Similar Network Traffic and Performance Evaluation. Wiley, New York, p. 39
Abry P., Flandrin P., Taqqu M. S., Veitch D., 2003, Theory and Applications of Long-Range Dependence. Birkhauser, Boston, p. 527
Addison P. S., 2002, The Illustrated Wavelet Transform Handbook. IOP Publishing, Bristol
Anzolin G., Tamburini F., De Martino D., Bianchini A., 2010, A&A, 519, A69
Bhat P. N., 2013, in Castro-Tirado A. J., Gorosabel J., Park I. H., eds, EAS Publ. Ser. Vol. 61, Temporal Decomposition Studies of GRB Lightcurves. Cambridge Univ. Press, Cambridge, p. 45
Coifman R. R., Donoho D. L., 1995, in Antoniadis A., Oppenheim G., eds, Lecture Notes in Statistics, Vol. 103, Translation-Invariant De-Noising. Springer-Verlag, 125
Feder J., 1988, Fractals. Plenum Press, New York
Flandrin P., 1992, IEEE Trans. Inf. Theory, 38, 910
Fritz T., Bruch A., 1998, A&A, 332, 586
Gao H., Lu Y., Zhang S. N., 2010, ApJ, 717, 268
Hakkila J., Nemiroff R. J., 2009, ApJ, 705, 372
Hakkila J., Preese R., 2011, ApJ, 740, 104
Horvath I., 1998, ApJ, 508, 757
Hurst H. E., 1951, Trans. Am. Soc. Civ. Eng., 116, 770
Kaplan L. C., Jay Kuo C. C., 1993, IEEE Trans. Signal Process., 41, 3554
MacLachlan G. A., Shenoy A., Sonbas E., Dhuga K. S., Eskandarian A., Maximon L. C., Parke W. C., 2012, MNRAS, 425, L32
MacLachlan G. A. et al., 2013, MNRAS, 432, 857
Mallat S. G., 1989, IEEE Trans. Pattern Anal. Mach. Intell., 11, 674
Mandelbrot B. B., van Ness J. W., 1968, SIAM Rev., 10, 422
Masry E., 1993, IEEE Trans. Inf. Theory, 39, 260
Meegan C. et al., 2009, ApJ, 702, 791
Nemiroff R. J., 2012, MNRAS, 419, 1650
Nemiroff R. J., 2000, ApJ, 544, 805
Norris J. P., Bonnell J. T., Kazanas D., Scargle J. D., Hakkila J., Giblin T. W., 2005, ApJ, 627, 324
Paciesas W. S. et al., 2012, ApJS, 199, 18
Percival D. B., Walden A. T., 2000, Wavelet Methods for Time Series Analysis. Cambridge Univ. Press, Cambridge
Scargle J. D., 1998, ApJ, 504, 405
Scargle J. D., Norris J. P., Jackson B., Chiang J., 2012, ApJ, 764, 167
Sonbas E., MacLachlan G. A., Shenoy A., Dhuga K. S., Parke W. C., 2013, ApJ, 767, L28
Tamburini F., De Martino D., Bianchini A., 2009, A&A, 502, 1
Walker K. C., Schaefer B., 2000, ApJ, 537, 264
Xizheng K., Zhensen W., 1997, Proc. IEEE Freq. Control Symp., On Wavelet Variance. p. 515

This paper has been typeset from a TeX/LaTeX file prepared by the author.